Available online at www.sciencedirect.com
ScienceDirect
Trans. Nonferrous Met. Soc. China 32(2022) 2391−2402
Transactions of Nonferrous Metals Society of China
www.tnmsc.cn

Application of suspension magnetization roasting as technology for high-efficiency separation of valuable iron minerals from high-iron bauxite

Ruo-feng WANG[1,2], Shuai YUAN[1,2,3], Peng GAO[1,2,3], Yan-jun LI[1,2,3]

1. School of Resources and Civil Engineering, Northeastern University, Shenyang 110819, China;
2. National-local Joint Engineering Research Center of High-efficient Exploitation Technology for Refractory Iron Ore Resources, Shenyang 110819, China;
3. State Key Laboratory of Rolling and Automation, Northeastern University, Shenyang 110819, China

Received 24 June 2021; accepted 17 March 2022

Abstract: A technology for suspension magnetization roasting−magnetic separation was proposed to separate iron minerals for recovery. The optimum parameters were as follows: a roasting temperature of 650 °C, a roasting time of 20 min, a CO concentration of 20%, and particles with a size less than 37 μm accounting for 67.14% of the roasted product. The total iron content and iron recovery of the magnetic concentrate were 56.71% and 90.50%, respectively. The phase transformation, magnetic transition, and microstructure evolution were systematically characterized through iron chemical phase analysis, X-ray diffraction, vibrating sample magnetometry, X-ray photoelectron spectroscopy, and transmission electron microscopy. The results demonstrated the transformation of hematite to magnetite, with the iron content in magnetite increasing from 0.41% in the raw ore to 91.47% in the roasted product.

Key words: high-iron bauxite; suspension magnetization roasting; comprehensive utilization; magnetic separation; phase transformation

1 Introduction

Aluminum and its alloys have essential applications in the construction machinery, transportation, aerospace, and military industries and other fields because of their favorable characteristics [1]. Bauxite is the primary source of aluminum [2,3]. According to the U.S. Geological Survey, there were 3×10^9 t of bauxite reserves worldwide and 3.71×10^8 t of bauxite produced in 2021. As the seventh-largest producer of bauxite globally, China contributes to the global primary aluminum capacity [4,5] and robust global alumina production and consumption [6−8].

High-iron bauxite is a typical refractory ore because of its complex composition and fine disseminated particle size. Aluminum and iron crystals have identical structural topologies [9]; therefore, ions in certain positions in the crystalline structure of one crystal can be easily replaced by those from another crystal, which makes the separation of iron minerals from bauxite tough by using a single process. Studies have shown that excessive iron minerals in bauxite ore are detrimental to alumina production [10−12], inevitably leading to large waste discharges and increasing the potential for water pollution [13−16]. As China's dependence on mineral resources has gradually increased, the principal barriers to further development of the steel and aluminum industries have been shortages of iron ore and bauxite [17,18]. If high-iron bauxite ore rich in iron minerals could be utilized effectively, it would significantly

Corresponding author: Shuai YUAN, Tel: +86-13234040556, E-mail: yuanshuai@mail.neu.edu.cn
DOI: 10.1016/S1003-6326(22)65955-7

increase aluminum and iron resources [19].

The economical and reasonable separation of iron minerals has always been a popular topic related to the research and development of high-iron bauxite, and has attracted the attention of researchers for a long time. Aluminum and iron separation methods can be subdivided into the biological [20−22], physical [23], acid leaching [24−26], and beneficiation-metallurgical methods. Biological methods involve microbial leaching [27,28]. Physical methods mainly include magnetic separation, flotation, and combined magnetic-floating methods, which are simple processes but achieve only a preliminary separation of iron and aluminum. Acid leaching can enrich the iron and aluminum components based on the difference in chemical properties between iron and aluminum minerals. However, acid leaching methods are expensive and cause environmental contamination. Beneficiation-metallurgical methods include the magnetization roasting and direct reduction technologies [29,30]. Magnetization roasting transforms weak magnetic iron minerals, such as hematite, siderite, and limonite, into magnetite or maghemite at a specific temperature and atmospheric pressure. The novel technology of suspension magnetization roasting (SMR) involves heating iron-bearing ore in a suspension-fluidized state, resulting in better gas–solid contact, higher heat, and higher mass transfer efficiency compared to conventional processes [31]. Long-term research on the development and utilization of high-iron bauxite resources has demonstrated that beneficiation-metallurgical methods for separating iron minerals from high-iron bauxite can achieve efficient results [32].

This study used SMR−magnetic separation technology to enrich and separate iron minerals from high-iron bauxite. A thorough investigation was conducted to determine the effects of the roasting temperature, roasting time, reduction atmosphere, and roasted product particle size on the experimental results. Moreover, X-ray diffraction (XRD), vibrating sample magnetometry (VSM), X-ray photoelectron spectroscopy (XPS), and transmission electron microscopy (TEM) were employed to determine the changes in micromorphology and phase transformation during SMR.

2 Experimental

2.1 Materials

High-iron bauxite ore was obtained from Shanxi, China. Details of the chemical composition of the raw ore are listed in Table 1. The ore was mainly composed of iron and alumina, with contents of 37.85% and 14.90%, respectively. Some other major chemical components found were CaO, TiO_2, and SiO_2, and the harmful elements S and P were less than 0.30%.

The results of the XRD analysis are presented in Fig. 1. The main minerals in the raw ore included diaspore, goethite, hematite, kaolinite, and calcite.

Table 1 Main chemical composition of raw ore (wt.%)

TFe	Al_2O_3	SiO_2	FeO	TiO_2	S	P	CaO	Na_2O	LOI
37.85	14.90	9.05	0.48	0.78	0.29	0.08	2.45	0.16	11.48

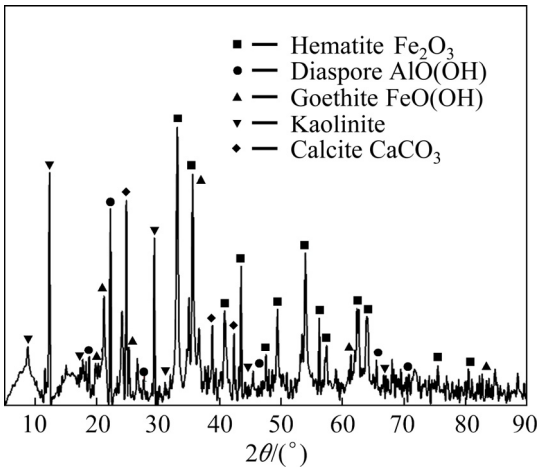

Fig. 1 XRD pattern of raw ore

According to Fig. 2, the iron chemical phase was analyzed using standard physical and chemical methods for mineral processing, including magnetic separation, acid leaching, and dissolution in aqua regia. As shown in Table 2, hematite and goethite were the dominant iron phases in the raw ore. The relative distribution of iron in the form of magnetite was 0.41%.

2.2 Equipment and procedures

Figure 3 shows the schematic diagram of the suspension magnetization roasting and magnetic separation experiments. The raw ore was ground and then screened, with 50% passing through a

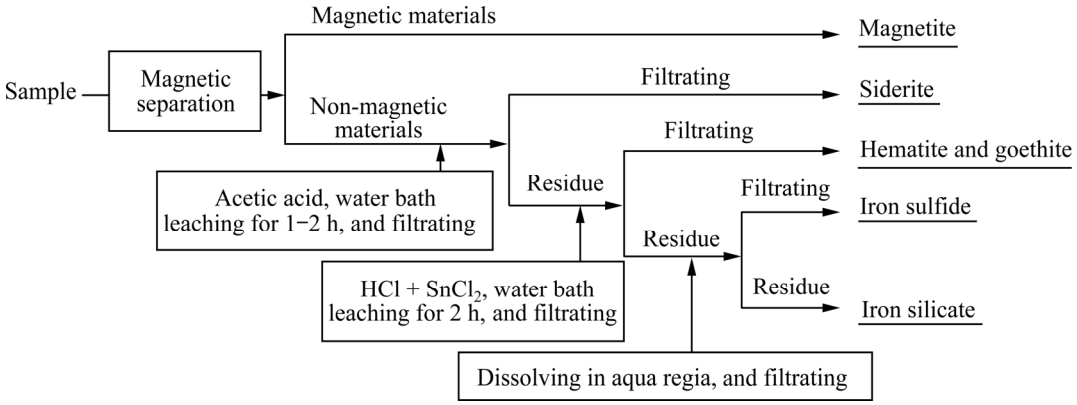

Fig. 2 Flow chart of iron chemical phase analysis

Table 2 Iron phases in raw ore

Fe phase	Content/wt.%	Distribution/wt.%
Magnetic Fe	0.16	0.41
Carbonate Fe	0.10	0.28
Oxide Fe	37.4	98.42
Sulfide Fe	0.13	0.34
Silicate Fe	0.21	0.55
Total Fe	38	100

45 μm sieve. After sample preparation, the specific test method was as follows.

Firstly, 25 g of high-iron bauxite was poured into a quartz tube to evenly distribute the bauxite across a porous quartz plate. Subsequently, high-purity N_2 was introduced at a flow rate of 600 mL/min, which facilitated the transformation of the samples into a fluidized state while removing the air in the tube. After the furnace temperature reached a predetermined value, the quartz tube was placed in the roasting furnace. Specific proportions of carbon monoxide and nitrogen were mixed using a gas mixing system and introduced into the quartz tube at a constant flow rate.

The carbon monoxide channel was closed to stop the reaction when the roasting time reached a predetermined value, but the nitrogen flow continued. The reactants remaining in the quartz tube were cooled to room temperature. The roasted product was removed from the tube and pulverized using a rod mill (XMB−70II). A magnetic separation tube (XCSG−120) was used to achieve low-intensity magnetic separation to produce a magnetic concentrate and non-magnetic product. These samples were analyzed to determine the alumina and iron contents.

2.3 Characterization methods

In this study, an automated XRD system (PW3040, Analytical B.V., Netherlands) was used for the XRD analysis, and scanning was performed for diffraction angles of 5°−90°. XPS was performed using an ESCALAB 250Xi X-ray photoelectron spectrometer with an Al K_α X-ray source (1486.6 eV photons). The XPS data were used for surface chemical analysis to detect the types of elements on the surface of the roasted product and the chemical state of the iron. The basic magnetic properties of the sample were measured using a JDAW−2000D high-sensitivity vibrating sample magnetometer. High-resolution TEM (HRTEM) images were obtained to characterize the raw ore and roasted product, and the morphology and crystal structure were evaluated using a JEOL 2100 microscope (Tokyo, Japan).

3 Results and discussion

3.1 Effects of roasting process parameters

3.1.1 Effects of roasting temperature

Temperature variations have a significant effect on roasting [33]. Experiments were carried out at temperatures ranging from 450 to 850 °C, with an increment of 50 °C. The other process parameters were as follows: a roasting time of 30 min, a total gas flow of 600 mL/min, and a CO concentration of 30%. After that, the roasted products were separated in a magnetic separation tube with a low magnetic field strength of 85 kA/m. The magnetic concentrate and tailing samples (non-magnetic product) were analyzed experimentally. Figure 4 presents the separation performance of the roasted products at different roasting temperatures.

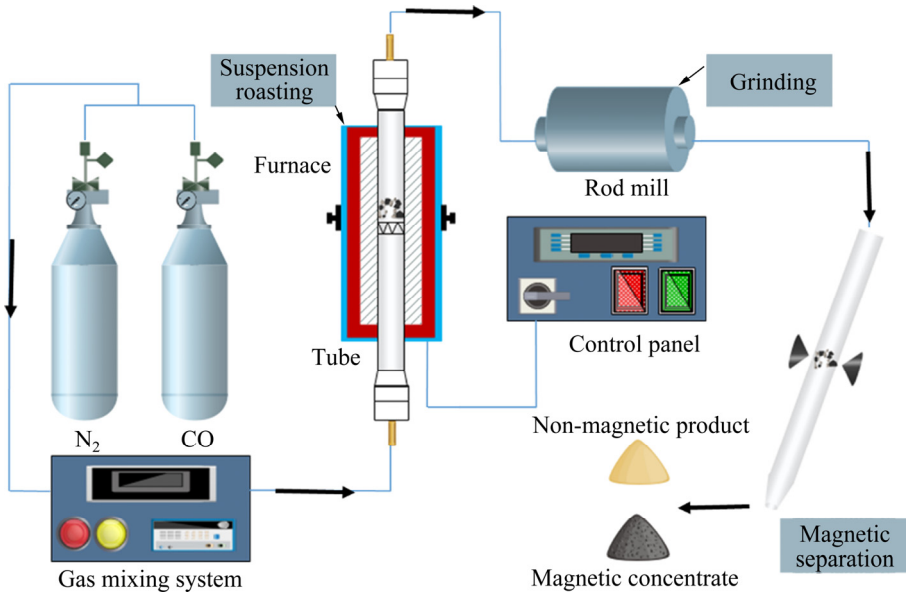

Fig. 3 Schematic diagram of suspension magnetization roasting and magnetic separation experiments

In Fig. 4(a), with an increase in roasting temperature from 450 to 650 °C, the iron content increased from 52.77% to 53.79%. However, the changes in the iron recovery and yield of the magnetic concentrate were not significant. As the temperature was further increased to 850 °C, the iron content increased. Nevertheless, there was a substantial decline in the yield of the magnetic concentrate, and the iron recovery decreased from 94.98% to 50.88 %. Similarly, Fig. 4(b) shows that as the temperature increased from 450 to 650 °C, the alumina content was stable at approximately 40%. In response to the increased roasting temperature, the aluminum content and iron recovery decreased due to weak magnetic ferrous oxide formation at high temperatures [34]. These results suggest that rigid roasting temperature control is a significant factor in the SMR process. The optimal roasting temperature was 650 °C.

3.1.2 Effects of roasting time

The roasting time significantly affected the separation of the roasted products [35]. After the optimal temperature was determined, the raw ore was roasted for 10, 20, 30, 40, and 50 min, respectively, at the optimal roasting temperature of 650 °C, a total gas flow rate of 600 mL/min, and a CO concentration of 30% to investigate and determine the effects of roasting time on the separation performance. The results are presented in Fig. 5.

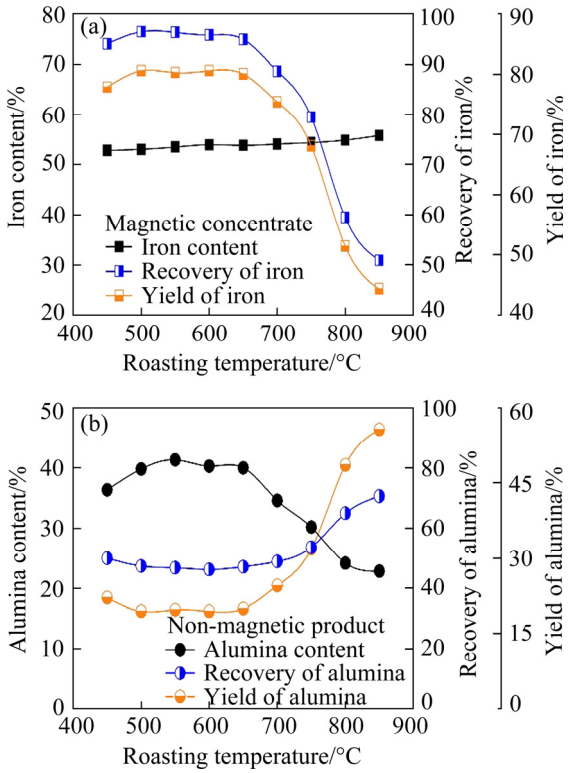

Fig. 4 Effects of roasting temperature on separation performance

Figure 5(a) shows that the iron recovery increased considerably when the roasting time was increased from 10 to 20 min. When the roasting time was further increased from 20 to 50 min, the iron recovery and yield of the magnetic concentrate showed no significant changes; however, the iron

content decreased from 53.45% to 52.35%. Similarly, when the roasting time was increased from 10 to 20 min, the alumina content effectively increased; however, the alumina content remained stable when the roasting time was increased further. Shorter roasting time resulted in the incomplete transformation of the hematite into magnetite. Nonetheless, after the complete reduction of the hematite, a further increase in the roasting time led to an over-reduction of iron minerals, thus reducing the quality of the roasted product. Therefore, a roasting time of 20 min was considered in subsequent experiments.

3.1.3 Effects of CO concentration

The gas concentration is also a dominant factor affecting SMR. Thus, the effects of the CO concentration on SMR were investigated within the range from 10% to 50%. The other process conditions were kept constant, i.e., the roasting time was 20 min, and the roasting temperature was 650 °C. The separation performance achieved in this experiment is shown in Fig. 6.

As shown in Fig. 6(a), the iron recovery remained stable. As the CO concentration increased, the yield of the magnetic concentrate gradually increased. When the CO concentration increased from 10% to 20%, the iron content did not change significantly, and as the CO concentration increased to 50%, the iron content decreased from 52.51% to 51.72%. It can be observed from Fig. 6(b) that changes in the CO concentration had a slight effect on the alumina content. However, an increase in the CO concentration resulted in a decrease in the yield of non-magnetic products. As the CO concentration increased from 10% to 20%, the alumina recovery decreased significantly from 45.32% to 43.17%, and the alumina recovery remained stable when the CO concentration exceeded 30%. An insufficient or excessive CO concentration substantially affected the iron content [36]. Therefore, the optimum CO concentration for subsequent experiments was determined to be 20%.

3.1.4 Effects of particle size

Particle size significantly impacted the roasted product when the SMR experiments were performed at a roasting temperature of 650 °C, a roasting time of 20 min, a stable total gas flow rate of 600 mL/min, and a CO concentration of 20%. The roasted products were ground using a rod mill and then separated in a magnetic separation tube.

The results in Fig. 7(a) suggest that when the mass fraction of particles smaller than 37 μm

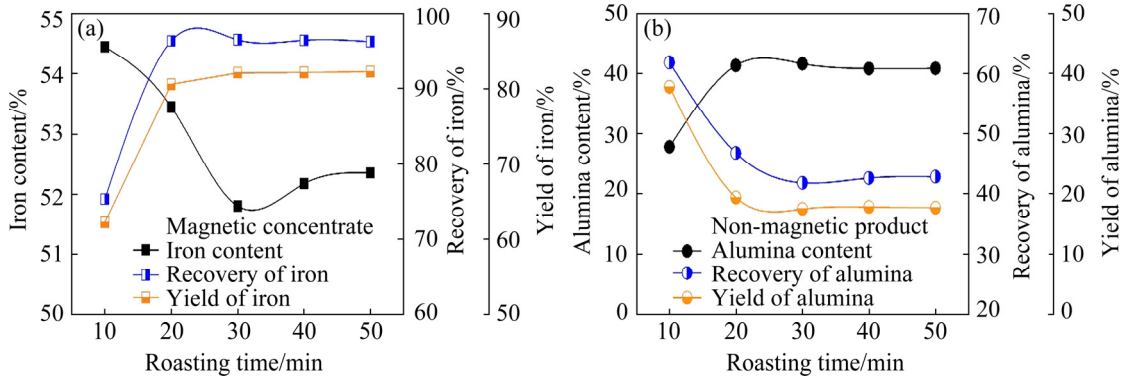

Fig. 5 Effects of roasting time on separation performance

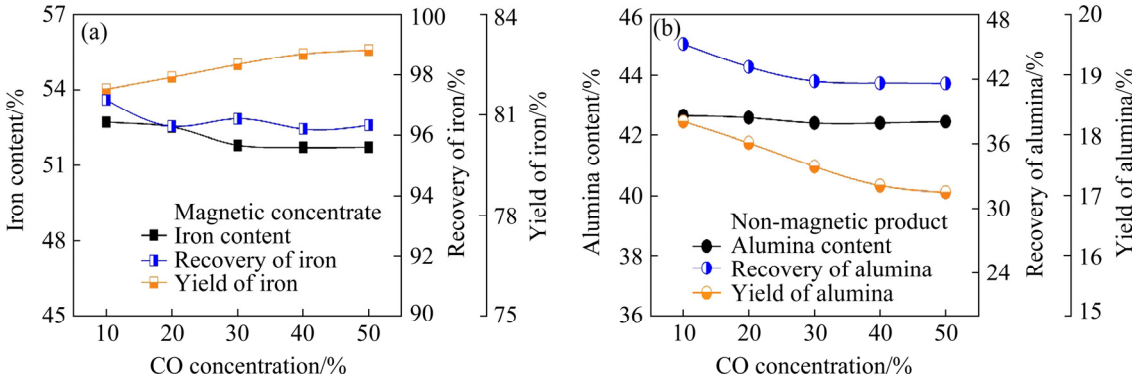

Fig. 6 Effects of CO concentration on separation performance

increased from 51.31% to 67.14%, the iron content increased from 56.12% to 56.71%. This indicates that an appropriate ground particle size could effectively facilitate the separation of iron from gangue minerals. Moreover, Fig. 7(b) shows that with a decrease in the ground particle size of the roasted product, when the mass fraction of particles smaller than 37 μm increased from 51.31% to 92.72%, the alumina content fluctuated within the range of 35.70%−40.18%, and the alumina recovery did not change noticeably. Therefore, the optimal ground particle size was less than 37 μm, and the particles accounted for 67.14% of the ore composition. In this case, the iron content and recovery of magnetic concentrate were 56.71% and 90.50%, respectively, and the alumina content of the non-magnetic product was 38.90%.

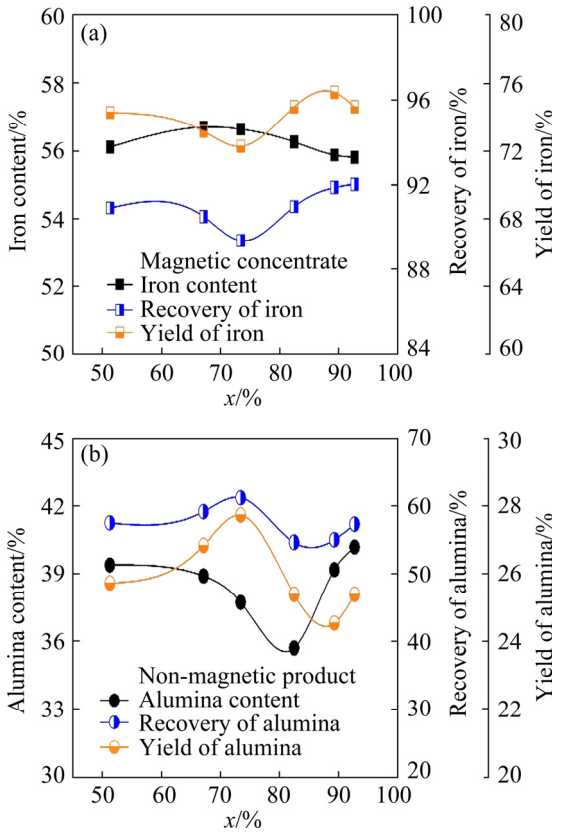

Fig. 7 Effects of particle size (mass fraction of particles less than 37 μm, x) on separation performance

3.2 Product characteristics

3.2.1 Chemical composition

The experiments were carried out under optimal experimental conditions, and the chemical compositions of the raw ore, the roasted product, the magnetic concentrate, and the non-magnetic product are shown in Fig. 8.

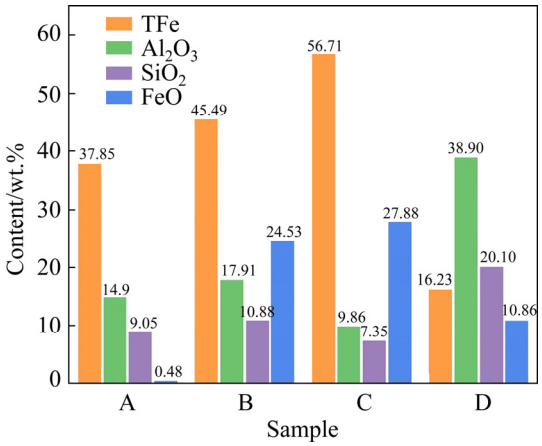

Fig. 8 Chemical compositions of samples at different roasting stages (A: Raw ore; B: Roasted product; C: Magnetic concentrate; D: Non-magnetic product)

The FeO content in the raw ore was only 0.48%, while that in the roasted product was 24.53%. This indicates that using SMR technology to transform iron mineral phases is feasible and effective. The iron content in the magnetic concentrate was 56.71%, available as a low-content iron concentrate for industrial smelting production. The non-magnetic product had an alumina content of 38.90% and can be used as a raw material for the Bayer process after desilication.

3.2.2 Phase transformation

The mineral phases present at different roasting stages were determined using XRD analysis. Figure 9 showed that the diffraction peaks attributed to hematite and goethite disappeared after SMR of the raw ore, while diffraction peaks attributed to magnetite appeared. These results can

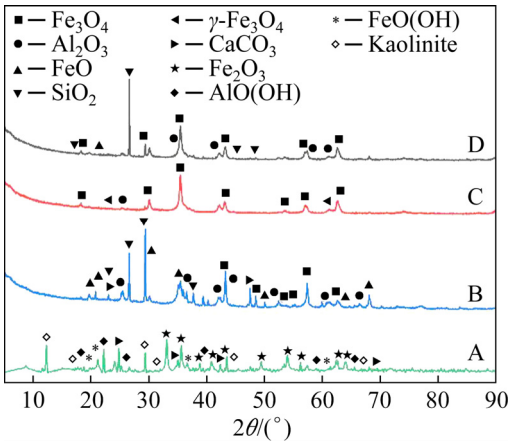

Fig. 9 XRD patterns of samples at different roasting stages (A: Raw ore; B: Roasted product; C: Magnetic concentrate; D: Non-magnetic product)

be ascribed to the transformation of hematite to magnetite after SMR. Figure 10 showed the same results, i.e., the iron-containing minerals in the raw ore mainly existed in the form of hematite and goethite, while magnetite accounted for only 0.41%. However, the iron chemical phase analysis of the roasted product showed that magnetite was the dominant phase, with a relative content of 91.47%. This indicates that the goethite and hematite in the raw ore were almost completely transformed into magnetite.

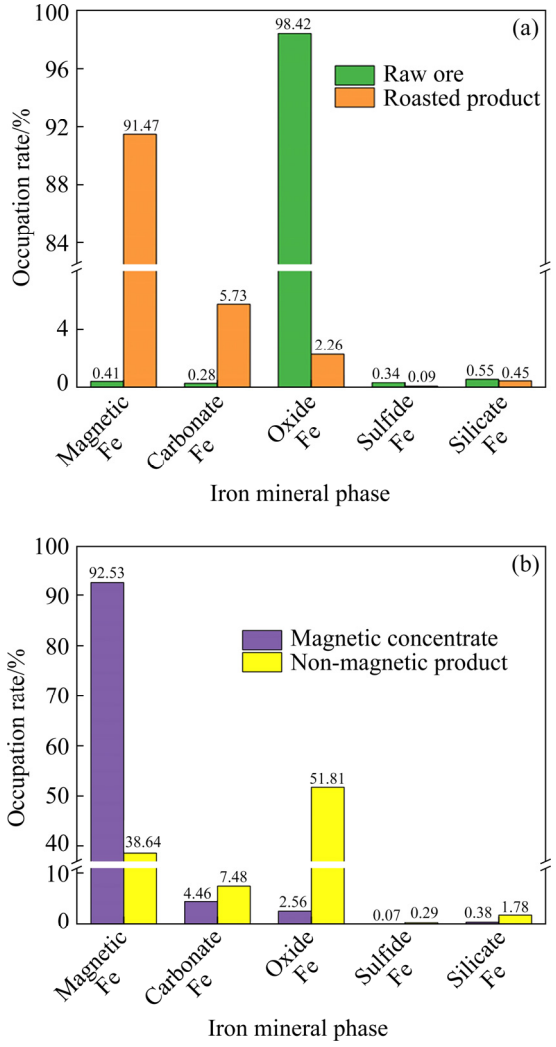

Fig. 10 Iron mineral phases of samples at different roasting stages

After roasting, the diffraction peaks attributed to the diaspore disappeared and were replaced by diffraction peaks attributed to alumina. XRD pattern of the magnetic concentrate demonstrated that the primary mineral was magnetite. Intense alumina peaks were observed in the XRD patterns of the non-magnetic product, while quartz and magnetite peaks were less. The above results prove that a magnetic separation process can efficiently separate iron and aluminum minerals after roasting.

3.2.3 XPS spectra

XPS is exceedingly sensitive to material surfaces, and chemical state changes on the mineral surface would significantly affect the shapes of the photoelectron peaks [37−40]. To further study the phase transformation of iron during SMR, XPS was used to characterize the surface chemical composition and chemical valence state of iron element in the raw ore, the roasted product, the magnetic concentrate, and the non-magnetic product. As illustrated in Fig. 11, XPS survey scans of the samples demonstrated the presence of Fe, O, Al, and Si. After SMR, the intensity of the Fe 2p peak increased; the detailed spectra are shown in Fig. 12.

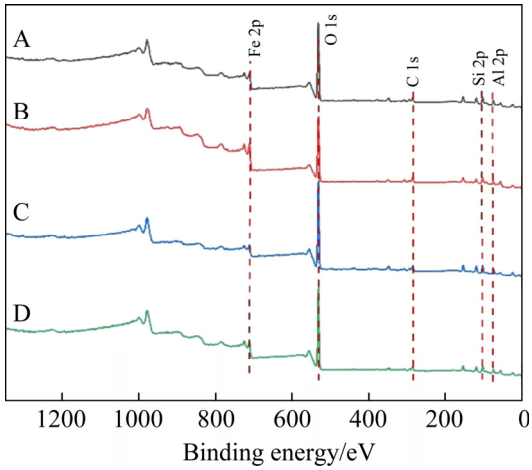

Fig. 11 XPS spectra of samples at different roasting stages (A: Raw ore; B: Roasted product; C: Magnetic concentrate; D: Non-magnetic product)

Figure 12(a) showed the detailed Fe 2p XPS spectrum of the raw ore, where the Fe $2p_{3/2}$ peak at a binding energy of 710.80 eV corresponds to Fe^{3+}—O bonds, and the Fe $2p_{1/2}$ peak at 724.00 eV corresponds to Fe^{3+}—O bonds. All the peaks showed that the Fe on the surface of the raw ore was in the form of Fe(III) and corresponded to the Fe_2O_3 phase, which was consistent with the XRD results shown in Fig. 9.

As seen in Fig. 12(b), the Fe 2p peak shifted significantly, with binding energies of 711.40 eV (Fe $2p_{3/2}$) and 723.50 eV (Fe $2p_{1/2}$). The results revealed that Fe^{2+} oxide was present in the roasted product; this indicated that the Fe(III) state was

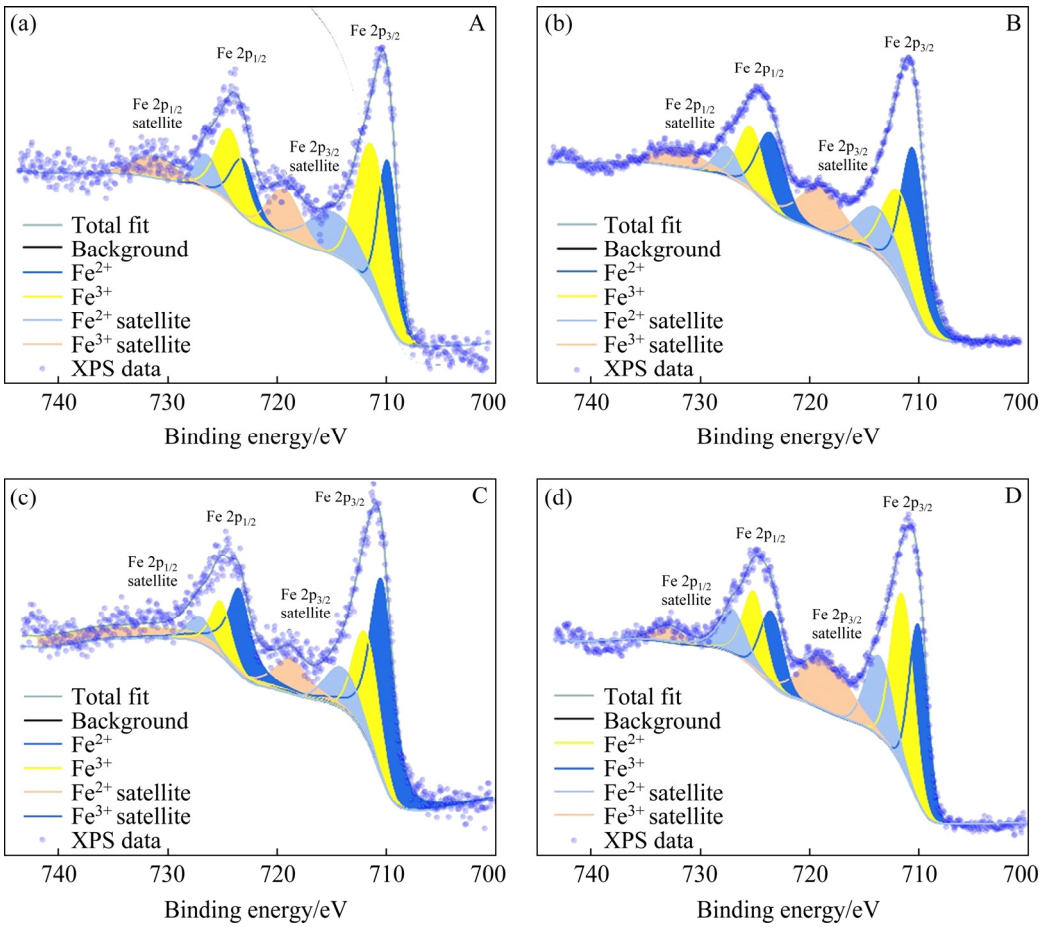

Fig. 12 Detailed XPS spectra of samples at different roasting stages (A: Raw ore; B: Roasted product; C: Magnetic concentrate; D: Non-magnetic product)

reduced to Fe(II), which demonstrated the presence of Fe_3O_4 (Fe_2O_3·FeO) [41]. Moreover, the area of the Fe(II) peak in the spectrum of the magnetic concentrate (Fig. 12(c)) was much larger than those in the spectra of the roasted product (Fig. 12(b)) and the non-magnetic product (Fig. 12(d)). These results provided sufficient proof that magnetite was enriched in the magnetic concentrate due to magnetic separation, which was consistent with the chemical iron phase results presented in Fig. 10.

In summary, the XPS results showed that Fe in the raw ore was in the form of Fe(III). After SMR, the amount of Fe in the form of Fe(II) substantially increased, providing tremendous evidence for phase transformation during SMR.

3.2.4 Magnetic characteristics

Studying the magnetic characteristics of the samples was essential to evaluate the reduction effects and reasonably select subsequent separation equipment and processes. The VSM results are presented in Fig. 13. These results showed that the unit mass magnetic moment of the four samples increased with increasing the external magnetic field intensity, and the specific magnetic susceptibility first increased rapidly and then decreased. When the applied magnetic field intensity was 6 MA/m, the unit mass magnetic moment of the raw ore, roasted product, magnetic concentrate, and non-magnetic product reached equilibrium at 0.026, 29.32, 36.88, and 7.46 $A·m^2/kg$, respectively.

The unit mass magnetic moment of the roasted product was significantly improved compared to that of the raw ore, which also demonstrated that the hematite in the raw ore was transformed into magnetite after SMR. The unit mass magnetic moment of the magnetic concentrate was higher than that of the roasted product, which could be attributed to the further enrichment of magnetite in the reduced product. According to the XRD analysis results, the non-magnetic product contained a small amount of magnetite, so the unit mass magnetic moment of the non-magnetic

product was significantly smaller but still showed a particular improvement compared with that of the raw ore.

3.2.5 TEM images

To further interpret the effects of SMR on the microscopic and crystalline structures of the iron phase, the raw ore and roasted product were analyzed using TEM and HRTEM, and the results are presented in Fig. 14.

Figures 14(a) and (d) show TEM images of the raw ore and roasted product, respectively. HRTEM images of the raw ore and roasted product are depicted in Figs. 14(b, c, e, f), which showed good crystallinity and clear lattice fringes of the minerals in the ore.

An examination of the mineral lattice parameters depicted in Figs. 14(b) and (c) revealed interplanar spacings of 0.252 and 0.270 nm, which are corresponding to the (110) and (104) planes of crystalline hematite, respectively, and an interplanar spacing of 0.498 nm corresponding to the (020) plane of crystalline goethite. The crystal fringes of two different minerals can be observed in the HRTEM results shown in Figs. 14(e) and (f). An investigation of the lattice parameters of magnetite showed lattice fringes with interplanar spacing values of 0.251, 0.242, and 0.210 nm, which corresponded to the (311), (222), and (400) planes of crystalline magnetite, respectively. In addition, the lattice spacing of wustite was 0.303 nm, which corresponded to the (204) plane of wustite.

Based on the TEM analysis results for the raw ore and roasted product, it can be concluded that SMR altered the microstructure and crystal phase of the iron phase, which was consistent with the XRD analysis results shown in Fig. 9.

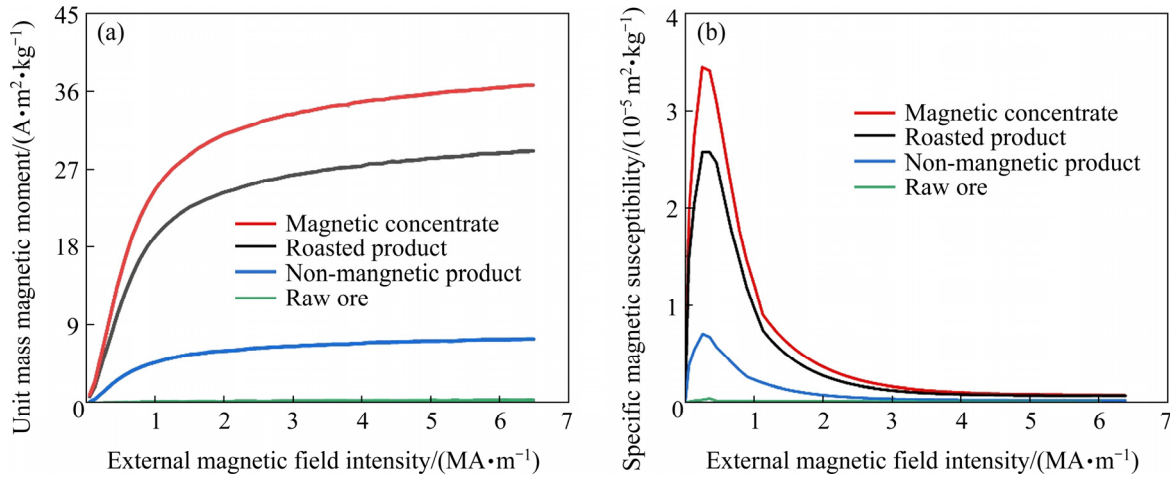

Fig. 13 Magnetic characteristics of samples at different roasting stages: (a) Unit mass magnetic moment; (b) Specific magnetic susceptibility

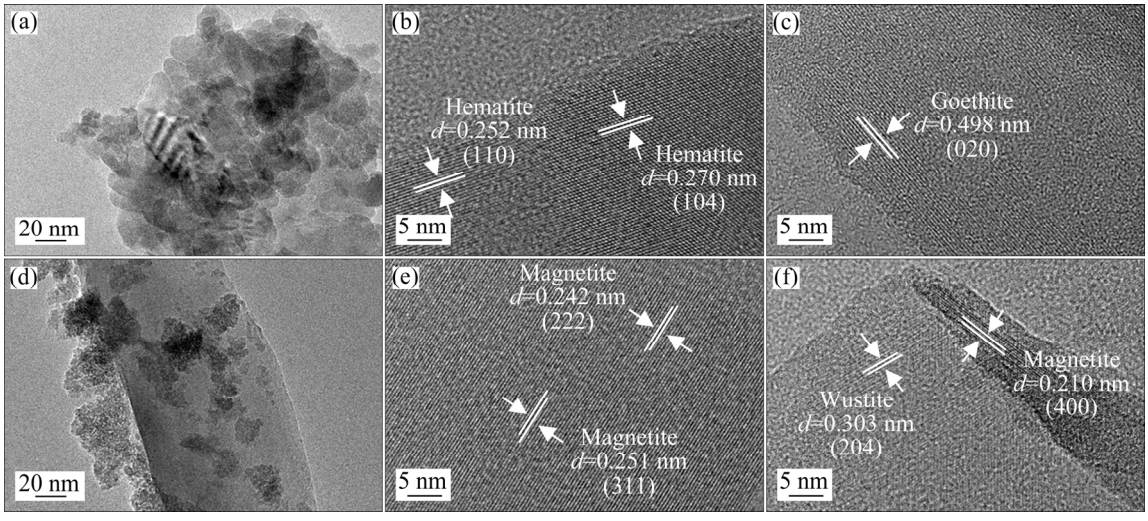

Fig. 14 TEM (a, d) and HRTEM (b, c, e, f) images for raw ore (a−c) and roasted product (d−f)

4 Conclusions

(1) Aluminum and iron minerals were separated from high-iron bauxite using SMR−magnetic separation technology under the optimal conditions of a roasting temperature of 650 °C, a roasting time of 20 min, a CO concentration of 20%, and a particle size of the roasted product less than 37 μm accounting for 67.14%. The iron recovery and iron content of the magnetic concentrate were 90.50% and 56.71% respectively, and the alumina content of the non-magnetic product was 38.90%.

(2) The XRD, XPS, and TEM analysis results demonstrated that the weakly magnetic hematite and goethite in the raw ore were transformed into strongly magnetic magnetite in the roasted products after SMR. This is beneficial to further enrichment of iron minerals.

(3) As illustrated by the VSM and iron chemical phase results, the iron content in magnetite increased from 0.41% in the raw ore to 91.47% in the roasted product, and the saturation magnetization of the magnetic concentrate was higher than that of the roasted product. The obtained magnetic concentrate could be considered a low-content iron concentrate for industrial smelting, and the non-magnetic product could be treated as a primary material for alumina production.

Acknowledgments

This research work was financially supported by the National Natural Science Foundation of China (Nos. 51904058, 52174240), and the Fundamental Research Funds for the Central Universities, China (No. 2101023).

References

[1] POP L D. Research on the optimal regime of recrystallization in 1050 aluminium alloy [J]. Procedia Manufacturing, 2019, 32: 4−7.

[2] ZHANG Ning-ning, NGUYEN A V, ZHOU Chang-chun. A review of the surface features and properties, surfactant adsorption and floatability of four key minerals of diasporic bauxite resources [J]. Advances in Colloid and Interface Science, 2018, 254: 56−75.

[3] KUAN S H, GHORBANI Y, CHIENG S. Narrowing the gap between local standards and global best practices in bauxite mining: A case study in Malaysia [J]. Resources Policy, 2020, 66: 101636.

[4] SUN Li, ZHANG Shuai, ZHANG Shi-hong, LIU Jian-nan, XIAO Ke-yan. Geologic characteristics and potential of bauxite in China [J]. Ore Geology Reviews, 2020, 120: 103278.

[5] YU Bi-ying, ZHAO Zi-hao, ZHANG Shuai, AN Run-ying, CHEN Jing-ming, LI Ru, ZHAO Guang-pu. Technological development pathway for a low-carbon primary aluminum industry in China [J]. Technological Forecasting and Social Change, 2021, 173: 121052.

[6] LI Shu-peng, NIU Li-peng, YUE Qiang, ZHANG Ting-an. Trajectory, driving forces, and mitigation potential of energy-related greenhouse gas (GHG) emissions in China's primary aluminum industry [J]. Energy, 2022, 239: 122114.

[7] CHEN Wei-qiang, SHI Lei. Analysis of aluminum stocks and flows in mainland China from 1950 to 2009: Exploring the dynamics driving the rapid increase in China's aluminum production [J]. Resources, Conservation and Recycling, 2012, 65: 18−28.

[8] DAI Min, WANG Peng, CHEN Wei-qiang, LIU Gang. Scenario analysis of China's aluminum cycle reveals the coming scrap age and the end of primary aluminum boom [J]. Journal of Cleaner Production, 2019, 226: 793−804.

[9] NEUMANN R, AVELAR A N, DA COSTA G M. Refinement of the isomorphic substitutions in goethite and hematite by the Rietveld method, and relevance to bauxite characterisation and processing [J]. Minerals Engineering, 2014, 55: 80−86.

[10] YUAN Shuai, XIAO Han-xin, YU Tian-yi, LI Yan-jun, GAO Peng. Enhanced removal of iron minerals from high-iron bauxite with advanced roasting technology for enrichment of aluminum [J]. Powder Technology, 2020, 372: 1−7.

[11] LI Lei, LIU Xiao-lian, WANG Gang, LIU Ya-lin, KANG Wei-min, DENG Nan-ping, ZHUANG Xu-pin, ZHOU Xing-hai. Research progress of ultrafine alumina fiber prepared by sol−gel method: A review [J]. Chemical Engineering Journal, 2021, 421: 127744.

[12] TIAN Tao, ZHANG Chao-lan, ZHU Feng, YUAN Shan-xin, GUO Ying, XUE Sheng-guo. Effect of phosphogypsum on saline-alkalinity and aggregate stability of bauxite residue [J]. Transactions of Nonferrous Metals Society of China, 2021, 31(5): 1484−1495.

[13] LI Xiao-bin, WANG Yi-lin, ZHOU Qiu-sheng, QI Tian-gui, LIU Gui-hua, PENG Zhi-hong, WANG Hong-yang. Transformation of hematite in diasporic bauxite during reductive Bayer digestion and recovery of iron [J]. Transactions of Nonferrous Metals Society of China, 2017, 27(12): 2715−2726.

[14] KANNAN P, BANAT F, HASAN S W, ABU HAIJA M. Neutralization of Bayer bauxite residue (red mud) by various brines: A review of chemistry and engineering processes [J]. Hydrometallurgy, 2021, 206: 105758.

[15] ZHANG Yong, GUO Zhao-hui, HAN Zi-yu, XIAO Xi-yuan. Effects of AlN hydrolysis on fractal geometry characteristics of residue from secondary aluminium dross using response surface methodology [J]. Transactions of Nonferrous Metals Society of China, 2018, 28(12): 2574−2581.

[16] LI Yi-wei, JIANG Jun, XUE Sheng-guo, MILLAR G J, KONG Xiang-feng, LI Xiao-fei, LI Meng, LI Chu-xuan.

Effect of ammonium chloride on leaching behavior of alkaline anion and sodium ion in bauxite residue [J]. Transactions of Nonferrous Metals Society of China, 2018, 28(10): 2125−2134.

[17] TIAN Ding, SHEN Xiao-yi, ZHAI Yu-chun, XIAO P, WEBLEY P. Extraction of iron and aluminum from high-iron bauxite by ammonium sulfate roasting and water leaching [J]. Journal of Iron and Steel Research International, 2019, 26(6): 578−584.

[18] LIU Zheng-gen, CHU Man-sheng, WANG Zheng, ZHAO Wei, TANG Jue. Study on metallized reduction and magnetic separation of iron from fine particles of high iron bauxite ore [J]. High Temperature Materials and Processes, 2017, 36(1): 79−88.

[19] ZHANG Yu-song, ZHANG Jie, WU Lin, TAN Lin, XIE Fei, CHENG Jiang-guo. Extraction of lithium and aluminium from bauxite mine tailings by mixed acid treatment without roasting [J]. Journal of Hazardous Materials, 2021, 404: 124044.

[20] LASKOU M, ECONOMOU-ELIOPOULOS M. The role of microorganisms on the mineralogical and geochemical characteristics of the Parnassos-Ghiona bauxite deposits, Greece [J]. Journal of Geochemical Exploration, 2007, 93(2): 67−77.

[21] BORRA C R, PONTIKES Y, BINNEMANS K, van GERVEN T. Leaching of rare earths from bauxite residue (red mud) [J]. Minerals Engineering, 2015, 76: 20−27.

[22] LIU Zhao-bo, ZONG Yan-bing, LI Hong-xu, JIA Dong-min, ZHAO Zi-han. Selectively recovering scandium from high alkali Bayer red mud without impurities of iron, titanium and gallium [J]. Journal of Rare Earths, 2017, 35(9): 896−905.

[23] HE Jing-feng, BAI Qiang, DU Tian-ye. Beneficiation and upgrading of coarse sized low-grade bauxite using a dry-based fluidized bed separator [J]. Advanced Powder Technology, 2020, 31(1): 181−189.

[24] RAO D S, RATH S S, DASH N, MOHANTY S, BISWAL S K. Mineralogy, liberation and leaching characteristics of iron oxide phases in an Indian diaspore sample [J]. Transactions of Nonferrous Metals Society of China, 2018, 28(8): 1640−1651.

[25] SWAIN R, RAO R B. Kinetic study on leaching of iron in partially laterised khondalite rocks for ceramic industrial applications [J]. International Journal of Mineral Processing, 2012, 112: 77−83.

[26] GUELFEN G, GUELFEN M, AYDIN A O. Dissolution kinetics of iron from diasporic bauxite in hydrochloric acid solution [J]. Indian Journal of Chemical Technology, 2006, 13(4): 386−390.

[27] KAHN H, TASSINARI M M L, RATTI G. Characterization of bauxite fines aiming to minimize their iron content [J]. Minerals Engineering, 2003, 16(11): 1313−1315.

[28] THELLA J S, MUKHERJEE A K, SRIKAKULAPU N G. Processing of high alumina iron ore slimes using classification and flotation [J]. Powder Technology, 2012, 217: 418−426.

[29] GU Fo-quan, LI Guang-hui, PENG Zhi-wei, LUO Jun, DENG Bo-na, RAO Ming-jun, ZHANG Yuan-bo, JIANG Tao. Upgrading diasporic bauxite ores for iron and alumina enrichment based on reductive roasting [J]. JOM, 2018, 70(9): 1893−1901.

[30] WU Hong-fei, CHEN Chao-yi, LI Jun-qi, LAN Yuan-pei, WANG Lin-zhu, QUAN Bian-li, JIN Hui-xin. Digestion mechanism and crystal simulation of roasted low-grade high-sulfur bauxite [J]. Transactions of Nonferrous Metals Society of China, 2020, 30(6): 1662−1673.

[31] CAO Yue, SUN Yong-sheng, GAO Peng, HAN Yue-xin, LI Yan-jun. Mechanism for suspension magnetization roasting of iron ore using straw-type biomass reductant [J]. International Journal of Mining Science and Technology, 2021, 31(6): 1075−1083.

[32] DENG Bo-na, LI Guang-hui, LUO Jun, YE Qing, LIU Ming-xia, RAO Ming-jun, JIANG Tao, BAUMAN L, ZHAO Bo-xin. Selectively leaching the iron-removed bauxite residues with phosphoric acid for enrichment of rare earth elements [J]. Separation and Purification Technology, 2019, 227: 115714.

[33] HE S C, WILSON B P, LUNDSTRÖM M, LIU Z H. Hazard-free treatment of electrolytic manganese residue and recovery of manganese using low temperature roasting−water washing process [J]. Journal of Hazardous Materials, 2021, 402: 123561.

[34] TANG Zhi-dong, GAO Peng, LI Yan-jun, HAN Yue-xin, LI Wen-bo, BUTT S, ZHANG Ya-hui. Recovery of iron from hazardous tailings using fluidized roasting coupling technology [J]. Powder Technology, 2020, 361: 591−599.

[35] ZHANG Tian-fu, LIU Wei, HAN Jun-wei, WU Gui-ting, JIAO Fei, QIN Wen-qing. Selective separation of calcium from zinc-rich neutralization sludge by sulfidation roasting and HCl leaching [J]. Separation and Purification Technology, 2021, 259: 118064.

[36] LIU Xiao, GAO Peng, YUAN Shuai, LV Yang, HAN Yue-xin. Clean utilization of high-iron red mud by suspension magnetization roasting [J]. Minerals Engineering, 2020, 157: 106553.

[37] WANG Xun, ZHAO Bing, LIU Jie, ZHU Yi-min, HAN Yue-xin. Dithiouracil, a highly efficient depressant for the selective separation of molybdenite from chalcopyrite by flotation: Applications and mechanism [J]. Minerals Engineering, 2022, 175: 107287.

[38] MEHDILO A, IRANNAJAD M. Surface modification of ilmenite and its accompanied gangue minerals by thermal pretreatment: Application in flotation process [J]. Transactions of Nonferrous Metals Society of China, 2021, 31(9): 2836−2851.

[39] LI Fang-xu, ZHOU Xiao-tong, LIN Ri-xiao. Flotation performance and adsorption mechanism of novel 1-(2-hydroxyphenyl)hex-2-en-1-one oxime flotation collector to malachite [J]. Transactions of Nonferrous Metals Society of China, 2020, 30(10): 2792−2801.

[40] YUAN Shuai, WANG Ruo-feng, GAO Peng, HAN Yue-xin, LI Yan-jun. Suspension magnetization roasting on waste ferromanganese ore: A semi-industrial test for efficient recycling of value minerals [J]. Powder Technology, 2022, 396: 80−91.

[41] OMRAN M, FABRITIUS T, ELMAHDY A M, ABDEL-KHALEK N A, EL-AREF M, ELMANAWI A E H. XPS and FTIR spectroscopic study on microwave treated high phosphorus iron ore [J]. Applied Surface Science, 2015, 345: 127−140.

高铁铝土矿悬浮磁化焙烧高效提铁技术

王若枫[1,2]，袁 帅[1,2,3]，高 鹏[1,2,3]，李艳军[1,2,3]

1. 东北大学 资源与土木工程学院，沈阳 110819；
2. 难采选铁矿资源高效开发利用技术国家地方联合工程研究中心，沈阳 110819；
3. 东北大学 轧制技术及连轧自动化国家重点实验室，沈阳 110819

摘 要：采用悬浮磁化焙烧−磁选技术对高铁铝土矿中铁矿物进行高效分离回收。在焙烧温度为 650 ℃、焙烧时间为 20 min、CO 浓度为 20%、焙烧产品粒度<37 μm 的含量为 67.14%的条件下，可获得总铁品位为 56.71%、铁回收率为 90.50%的磁选精矿。采用铁化学物相分析法、X 射线衍射仪、振动样品磁强计、X 射线光电子能谱仪和透射电镜等研究焙烧过程中矿物物相转变、磁性特征和显微组织演变规律。结果表明，原矿中赤铁矿转变为磁铁矿，磁性铁含量由原矿的 0.41%提高到焙烧产品中的 91.47%。

关键词：高铁铝土矿；悬浮磁化焙烧；综合利用；磁选；物相转化

(Edited by Wei-ping CHEN)